Research Square

Preprints are preliminary reports that have not undergone peer review.
They should not be considered conclusive, used to inform clinical practice,
or referenced by the media as validated information.

Systematic identification of synergistic combinations of targeted agents and immunotherapies in breast cancer using intratumor multiplex implantable microdevice assay

Zuzana Tatarova
Harvard Medical School
Dylan Blumberg
Oregon Health & Science University
James Korkola
Oregon Health and Science University
Laura Heiser
Department of Biomedical Engineering, Oregon Health Sciences University https://orcid.org/0000-0003-3330-0950
John Muschler
Oregon Health & Science University
Pepper Schedin
Oregon Health and Science University https://orcid.org/0000-0003-4244-987X
Sebastian Ahn
Harvard Medical School
Gordon Mills
Oregon Health and Science University https://orcid.org/0000-0002-0144-9614
Lisa Coussens
Oregon Health Sciences University https://orcid.org/0000-0003-2389-1865
Oliver Jonas
Harvard Medical School
Joe Gray (grayjo@ohsu.edu)
Oregon Health and Science University https://orcid.org/0000-0001-9225-6756

Article

Keywords: breast cancer, synergistic combinations, long-term breast cancer control

Posted Date: November 24th, 2021

DOI: https://doi.org/10.21203/rs.3.rs-1054728/v1

License: This work is licensed under a Creative Commons Attribution 4.0 International License.
Read Full License

Version of Record: A version of this preprint was published at Nature Biotechnology on July 4th, 2022.
See the published version at https://doi.org/10.1038/s41587-022-01379-y.

Systematic identification of synergistic combinations of targeted agents and immunotherapies in breast cancer using intratumor multiplex implantable microdevice assay

Zuzana Tatarova,[1,2,3] Dylan C. Blumberg,[1] James E. Korkola,[1,2] Laura M. Heiser,[1,2] John L. Muschler,[1,2] Pepper J. Schedin,[2,4] Sebastian W. Ahn,[3] Gordon B. Mills,[5] Lisa M. Coussens,[2,4] Oliver Jonas,[3,*] Joe W. Gray[1,2,*]

[1]Department of Biomedical Engineering, OHSU Center for Spatial Systems Biomedicine
[2]Knight Cancer Institute
Oregon Health & Science University, Portland, OR 97239, USA
[3]Department of Radiology, Brigham & Women's Hospital
Harvard Medical School, Boston, MA 02115, USA
[4]Department of Cell and Developmental Biology
[5]Division of Oncologic Sciences
Oregon Health & Science University, Portland, OR 97239, USA
*Correspondence: ojonas@harvard.bwh.edu (O.J.), grayjo@ohsu.edu (J.W.G.)

Abstract

Systematically identifying synergistic combinations between targeted agents and immunotherapies in cancer based on genomic or other static biomarkers remains elusive. Here we integrate two novel high-content and high-throughput techniques, an implantable microdevice to administer multiple drugs into different sites in tumors at nanodoses; and spatial systems analysis of tumor microenvironmental states to describe tumor cell and immunological response signatures and rapidly, within days, identify effective combinations from among numerous agents. We demonstrate in systemic follow-up studies across three mammary carcinoma models that combinations identified by this approach lead to highly synergistic effects. Biomarkers associated with resistance to each agent allowed us to prioritize at least five novel treatment strategies of which the panobinostat/venetoclax/anti-CD40 was the most effective inducing complete tumor control across models. We show that spatial association of

cancer stem cells with dendritic cells during immunogenic cell death is a potential mechanism of action underlying long-term breast cancer control.

Introduction

Modern cancer therapies increasingly seek to effect tumor control by simultaneously attacking tumor intrinsic vulnerabilities, enhancing anti-tumor immune activity and/or mitigating stromal mediators of resistance. Targeted drugs typically are designed to attack genetic or transcriptional vulnerabilities on which tumor cells depend for survival but non-malignant cells do not[1]. Genomic screening approaches have supported such tumor-intrinsic aspects of precision medicine, leading to matching of genomic aberrations with specific targeted agents[2]. In breast cancer, treatments targeting tumors that depend on estrogen receptor (ER) signaling, aberrant signaling resulting from human epidermal growth factor receptor 2 (HER2) amplification and/or over expression, CDK4/6 signaling and defects in DNA repair in triple negative breast cancer (TNBC) have been particularly effective[3]. Unfortunately, these treatments are not uniformly effective even in primary tumors carrying the target and are usually only transiently effective in metastatic disease[4,5]. This may be due in part to drug modulation of aspects of the tumor microenvironment (TME) suggesting that treatment efficacy can be increased by combing these drugs with agents that increase immunogenicity and/or counter microenvironment-mediated resistance, a hypothesis that we address in this paper.

The concept of enhancing cancer treatment efficacy by combining chemotherapies and targeted drugs with agents that enhance immune mediated anti-tumor activity is increasingly well established[6]. The clearest example is the use of immunotherapies, including immune checkpoint blocking (ICB) antibodies as complements to tumor targeted therapies in various liquid and solid malignancies[7]. However, many cancers do not benefit from ICB including in breast cancer where efficacy has been limited to a subset of TNBC patients[8,9]. This lack of efficacy has been attributed, in part, to low tumor mutational burden[10] and to two mechanisms: i) Low antigenicity through decreased expression of major histocompatibility complex class I (MHC-I) proteins - observed mainly in luminal ER+ BC[4,11] and HER2+ BCs[12,13]; and ii) a naturally immunosuppressive TME associated mainly with TNBC and HER2+ BC[14,15]. Both of these mechanisms may limit CD8+ T cell-mediated anti-tumor responses, which then cannot be leveraged to improve efficacy of ICB therapies[16]. Combinations of conventional chemotherapies

and/or targeted anticancer drugs that increase immunogenic cell kill promise significant improvements in overall outcome[17,18]. However, further understanding of drug-immune system interactions is required to design effective and safe immune modulating combinatorial regimens.

A variety of experimental approaches have been deployed to elucidate the effects of drug combinations on the tumor and stromal components and to identify biomarkers that inform on the efficacy of treatment combination decisions[1]. Biomarkers typically are identified by establishing associations between tumor features and outcomes in clinical studies[10] such as those supported by the NCI National Clinical Trials Network[19], The Cancer Genome Atlas[20] and Human Tumor Atlas Network[21] programs. However, these association-based approaches need to be tested for causality in systems that faithfully recreate the interactions of the various components of the TME. Common model systems include tumors that arise in immune competent mice and short- or long-term ex vivo cultures comprised of tumor and stromal components using miniscule scaffolds and active fluidics to closely model specific aspects of the TME[22,23]. However, the whole animal mouse studies typically are slow, expensive and labor-intensive, and comprehensive modeling and faithful recapitulation of TME interactions in ex vivo systems remains a major challenge[24].

We report now on an integrated *in vivo* approach to rapidly, safely and efficiently assess the effects of multi-drug treatments on the TME composition and architecture in living mice. Our study focuses on mouse mammary cancers and our approach is based on the intratumor delivery of nanoliter doses (nanodoses) of multiple drugs or drug combinations into spatially separate regions of a tumor using a minimally invasive, implantable microdevice (IMD)[25–27] and multiplexed immunohistochemical (mIHC) assessments[28,29] of the in-situ responses of the tumor-microenvironment milieu near each drug delivery site. Computational analyses of serial mIHC staining and imaging of 30+ proteins allow precise characterization of tumor cell states (e.g. proliferation, stemness, antigenicity, apoptosis) as well as comprehensive classification of cells comprising the TME including immune cells, vasculature and other stroma cells. Assessment of the composition and spatial distribution of the functionally different cell types in each drug delivery area facilitates identification of drug-mediated mechanisms of response and resistance that suggest new therapeutic interventions. We refer to this approach as the Multiplex Implantable Microdevice Assay (MIMA) and we used it to evaluate the effects of five targeted anticancer agents (olaparib, palbociclib, venetoclax, panobinostat, lenvatinib) and two

chemotherapies (doxorubicin, paclitaxel) to predict synergistic anti-tumor effects with different immune-based therapies. The data predicted that palbociclib would synergized with anti-CSF1R, venetoclax with anti-CD40 and panobinostat with anti-PD-1 immunotherapy, respectively, which we validated in traditional systemic dosing studies. We found the triple combination of panobinostat, venetoclax and anti-CD40 as curative and well-tolerated across multiple models of mammary cancer with immunogenic cell death and spatial association of dendritic cells with cancer stem cells representing the likely mechanism underlying cancer stem cell specific anti-tumor immunity in breast cancer.

Results

MIMA components and design

The IMD used for drug delivery in the MIMA system was a 5 mm long, 0,75 mm diameter biocompatible resin cylinder that delivered multiple drugs or drug combinations in up to 18 spatially separate regions inside a living tissue (Fig. 1a). IMDs were loaded with drugs formulated with poly-ethylene glycol (PEG) in semi-solid form so that drugs are released with controlled kinetics upon implantation via passive diffusion[25]. Local concentrations of drugs in the IMD were tuned to produce drug levels at each site in the tissue that recapitulate those achieved during systemic treatment (Extended Data Fig. 1a and Supplementary Table 1). Importantly, the nanodoses of drugs do not generate the whole animal toxicities typically associated with systemic treatments[25].

After treatment for 3 days, tumors were harvested with the IMD in place, prepared as a formalin fixed, paraffin embedded (FFPE) samples and serial tissue sections were cut orthogonal to the axis of the IMD (Fig. 1a). Sections through each drug delivery well were stained using mIHC – a process of serial immunostaining, imaging and stripping (Fig. 1b and Extended Data Fig. 1b, c)[28,29] – to assess local drug effects using a range of markers with specific staining patterns being cross validated against those generated using cyclic immunofluorescence (cycIF)[28] (Extended Data Fig. 1c-f). The-mIHC generated multiprotein images were then analyzed by segmenting individual cells and calculating protein expression levels in each segmented cell (Fig. 1c and Extended Data Fig. 2). For our MIMA studies we developed a comprehensive mouse specific readout panel including 30+ proteins (Fig. 1d and Supplementary Table 2, 3) with the criteria to

(i) interrogate a broad range of tumor and TME states and functions and (ii) to identify actionable phenotypes with preferential detection of early and local responses. We selected 13 proteins (Epcam, CD45, CD31, αSMA, CD3, CD4, CD8, CD11b, F4/80, CSF1R, CD11c, Ly6G, MHC-II; Fig. 1a, baseline discovery panel) to classify 17 "standard cell types" which were essential and satisfactory to capture major TME states predicting effective treatment combinations (Fig. 1e-g and Supplementary Table 4). We interrogated additional proteins to refine the 17 standard cell types and/or to report on basic drug sensitivity (proliferation, apoptosis), immunogenic cell death and/or processes typically associated with resistance such as cancer stem cells (Fig. 1d; extended readout).

MIMA identifies drug specific histological signatures of TME response predicting rational treatment combinations

We used the MIMA system to perform a small-scale *in situ* screen and quantitatively assess responses to seven FDA approved drugs with distinct modes of action. The targeted drugs were the poly (adenosine diphosphate [ADP]) ribose polymerase (PARP) inhibitor, olaparib; the multi-kinase vascular endothelial growth factor receptor (VEGFR)-1/2/3 inhibitor, lenvatinib; the cyclin dependent kinase (CDK)-4/6 inhibitor, palbociclib; the B-cell lymphoma (BCL)-2 inhibitor, venetoclax; and the pan- histone-deacetylase (HDAC) inhibitor, panobinostat. The chemotherapeutic drugs were the DNA-intercalating agent, doxorubicin and the mitotic inhibitor, paclitaxel that are often used in first line therapy for BCs[30]. We assessed the responses in tumors arising in immunocompetent MMTV-PyMT (mouse mammary tumor virus-polyoma middle tumor-antigen) mice – a commonly used genetically engineered mouse model for breast cancer that mirrors many aspects of human breast cancer progression and heterogeneity[31,32]. We chose a spontaneous rather than transplanted tumor model to better account for all stages of immune-biology associated with de novo tumor progression[33], including editing[34].

Our analyses of harvested tumors focused on the cell and molecular compositions and organizations that were significantly enriched in regions close to the drug delivery sites compared to distant intratumoral controls (Fig. 1h). The changes observed for our 17 standard cell types are summarized in Fig. 1g for all seven drugs and Figs. 1i-l show computed images of selected cell types after treatment.

Lenvatinib and paclitaxel produced no detectable effects and they resembled those produced by PEG negative control (Fig. 1g, i and Extended Data Fig. 3a-c); while olaparib caused only a modest increase in macrophage, neutrophil and fibroblast number (Fig. 1g). Doxorubicin did not mediate immune changes, but did cause a significant enrichment of endothelial cells (Fig. 1g and Extended Data Fig. 3d) suggesting that normalization of vasculature[35,36] could increase efficacy of doxorubicin in breast cancer. Palbociclib, venetoclax, and panobinostat produced the strongest changes in the immune and non-immune stromal states (Fig. 1g, j, k l). We extended mIHC analytics and performed spatial cell measurements to describe the mechanism of action of these drugs in more detail.

Palbociclib induces enrichment of CSF1R+ macrophages associated with pericyte branching and de novo tumor proliferation

Intratumoral treatment with palbociclib induced significant accumulation of several stromal cell types into the assay area including CSF1R-positive, MHC-II negative pro-tumorigenic macrophages[6], endothelial cells, vascular pericytes and mesenchymal cells (Fig. 1g, j; 2a, b and Extended Data Fig. 4a-c). Spatial analyses measuring relative abundance of cells at increasing distances from the drug delivery well showed that while the CD45+ macrophages – as classified by standard cell type – were localized to regions immediately proximal to the drug delivery well; the CD45- less-differentiated macrophages[37,38] were localized both proximally and more distally (Fig. 2c, d) and in some regions were associated with contractile pericytes[36] (Fig. 2d). We also assessed the propensity of specific cell types to cluster together by mapping the locations where 10 or more cells of a defined phenotype occurred together in regions 30, 50 or 75 μm in diameter (Fig. 2e and Extended Data Fig. 4d). These analyses showed that the CSF1R+ macrophages and CD31+ endothelial cell/pericyte structures were organized together in response to palbociclib drug stimulus and did not appear in PEG control tissues (Fig. 2e). The patterns for the CD31+ cell aggregates were branch-like with pericytes integrated within endothelial structures suggestive of large vessel formation and enhanced blood flow/pressure control[36] (Fig. 2e and Extended Data Fig. 4d). The profile plot and distance-based cluster analyses also showed clusters of Ki67-positive neoplastic cells distant from the drug delivery site and proximal to the macrophage-pericyte networks (Fig. 2d, e and Extended Data Fig. 4b, d) indicating that the macrophage-pericyte structures likely contribute to an increase in tumor cell proliferation in local

183 microculture as summarized schematically in Fig. 2f. These results provide direct evidence of
184 how specific changes in tumor microenvironmental states induced by monotherapy may mediate
185 acquired resistance. The high expression of CSF1R on multiple cell types (Fig. 2c) and the
186 associated increase in Ki67+ tumor cells (Fig. 2d-e) suggested to us that targeting the
187 CSF1/CSF1R axis might enhance palbociclib efficacy by countering CSF1R-mediated processes
188 (Supplementary Table 4).

189 We tested this concept in a systemic study of the EMT6 breast cancer model, by treating mice
190 bearing tumors orthotopically implanted into the mammary fat pads of immunocompetent
191 syngeneic mice with intraperitoneal injections of palbociclib, an anti-CSF1R antibody
192 monotherapy, and a combination of the two. The individual drugs did not affect the rate of tumor
193 growth. However, the combination treatment significantly reduced tumor growth (Fig. 2g). Thus,
194 the efficacy of palbociclib/anti-CSF1R suggested by analyses of responses to intratumoral
195 treatments was confirmed in whole animal experiments.
196
197 **Venetoclax recruits phenotypically distinct clusters of dendritic cells, immature myeloid**
198 **cells and endothelial cells**

199 Intratumor treatment with venetoclax resulted in significant recruitment of CD11c+ dendritic
200 cells (DCs), immature myeloid cells and CD31+ endothelial cells to the drug assay area (Fig.
201 1g,k; Fig. 3a and Extended Data Fig. 4e, f). Unlike in the palbociclib condition, the CD31+
202 endothelial cells did not express αSMA suggesting they formed small blood vessels that were
203 not supported by pericytes[36] (Fig. 3b). CD11c+ DCs, which play a critical role in regulating the
204 balance between immune tolerance and activity[39], aggregated into multiple, spatially separate
205 clusters in regions near venetoclax delivery, but not in random intratumoral regions far from the
206 drug releasing site (Fig. 3c). The clusters were phenotypically distinct as defined by their
207 morphology (Fig. 3d) and expression of Epcam, CD45, MHC-II and CD11b (Fig. 2e). DCs
208 closer to the reservoir exhibited brighter and smaller nuclei (Fig. 3d, 1) and greater than 60%
209 were Epcam+, CD45- (Fig. 2e) suggesting that they were phagocytic[40]; while others displayed a
210 "Bull's-eye" membrane CD45 staining pattern typical of unstimulated myeloid cells[40] (Fig. 3d,
211 4). However, only a small fraction of these cells, which were spatially associated with
212 endothelial cells (Fig. 2d, 3), were MHC-II positive (Fig. 3e) and thus were likely limited in their

ability to present available tumor antigens[41]. Agonist monoclonal anti-CD40 antibodies can act on DCs and immature myeloid cells to increase their antigen presenting capacity, maturation and activation potential (called licensing) thereby shifting the balance from tolerance to anti-tumor immunity[39,42,43]. We reasoned that this immunotherapy could be used to enhance anti-tumor capacity of the immune cells recruited by venetoclax which were already primed to have antitumor activity (Fig. 3f).

Our test of this hypothesis by systemic treatment of the E0771 orthotopic breast cancer model with a combination of venetoclax and an anti-CD40 agonist showed that this combination reduced tumor growth rate and increased overall survival with 60% of mice surviving for >180 days (Fig. 3g). For comparison, the combination of venetoclax with a programmed death ligand-1 (PD-1) inhibitory antibody did not significantly affect tumor growth rate or survival (Fig. 3g). Again, a therapeutic strategy suggested by the MIMA proved to be effective in whole animal experiments.

Panobinostat induces immunogenic cell death associated with recruitment of antigen presenting neutrophils and macrophages

Intratumor delivery of panobinostat led to significant recruitment of several immune cell populations including dendritic cells, antigen presenting macrophages and (antigen presenting) neutrophils with the latter being the most abundant (Fig. 1g, l; 4a, b and Extended Data Fig. 5a-c).

Neutrophils are considered to be rapid responders against pathogens and classically are not categorized as professional antigen presenting cells as compared to DCs, B-cells, monocytes and macrophages, which have superior ability to prime naïve T cells[41]. However, 13% of neutrophils were MHC-II-positive (Fig. 4c, d) suggesting had undergone strong phenotypic maturation[44]. MHC-II+ neutrophils have recently been linked to immunogenic cell death (ICD) during which they phagocytose dying tumor cells and mediate respiratory-burst-dependent cytotoxicity against residual cells[44]. Interestingly, panobinostat induced the highest cell kill among the seven drugs tested (Fig. 4e, f). Based on our observation of significant enrichment of MHC-II+ antigen presenting neutrophils associated with cell death, we hypothesized that panobinostat-mediated

cell death would be immunogenic and the efficacy of this targeted therapy would be enhanced by PD-1 blockade.

Systemic treatment of EMT6 and E0771 model tumors with panobinostat plus anti-PD-1 increased survival duration and reduced tumor growth rate relative to treatment controls or to treatment with panobinostat alone (Fig. 5g) indicating effective induction of antitumor immunity. Consistent with this, systemic treatment with panobinostat significantly increased the proportion of intratumoral CD8+ T cells as compared to stromal parenchyma (Extended Data Fig. 5d). However, the treatments did not achieve long term tumor control (Fig. 5c), and in vaccination studies[45], only a subset of mice in both EMT6 and E0771 models rejected the tumor post re-challenge (Fig. 4i). These results suggest that resistance mechanisms exist that might counter the full potential of panobinostat-mediated antitumor immunity, and thus we explored this treatment condition in more detail.

Biomarkers of response and mechanisms of resistance associated with early induced anti-tumor immunity in breast cancer

Through literature review, we generated a list of early *in situ* biomarkers which have been directly or indirectly linked to ICD, increased tumor CD8+ T cell infiltrate and/or ICB efficacy. These include: intercellular adhesion molecule 1 (ICAM1)[46,47], myeloperoxidase (MPO)[47], calreticulin[17,18,48], MHC-I[49,50], galectin-3[46,51], neuropilin-1[52,53] and PD-L1[8,9]. We validated the presence of these biomarkers at panobinostat reservoirs (Fig. 5a and Extended Data Fig. 6a) and measured their expression and spatial association in relation with the standard stromal cell types in the assay area (Fig. 5b) as well as cancer stem cells (CSCs, Epcam-CD45+PyMT+Ki67-Sox9+) (Fig. 5c-f) – a subset of tumor cells that have self-renewal and tumor initiating capacity which often exhibit resistance to anti-cancer treatments[5,54,55].

ICAM1, MPO and Neuropilin-1 were localized in the *proximal* cell death and neutrophils rich assay region; while PD-L1, galectin-3, MHC-I and calreticulin were localized mostly on tumor cells *distal* from the well with the latter two having decreasing gradient profile (Fig. 5a and Extended Data Fig. 6a). A majority (65%) of Ly6G+ neutrophils were positive for MPO (Extended Data Fig. 6b) consistent with cytotoxic capacity. Positivity for ICAM1 (Fig. 5b) and the mutually exclusive expression of the immune suppressive molecule arginase-1 on this

population (Extended Data Fig. 5b and 6a) indicate these are anti-tumor (reported also as N1) rather than protumor (N2) neutrophils[56]. Co-treatment with panobinostat and an anti-Ly6G antibody decreased panobinostat mediated cell death implying that these neutrophils may have tumor-killing function as a result of the drug's mechanism of action (Extended Data Fig. 6c). The vast majority (up to 88%) of neuropilin-1 positive cells proximal to the panobinostat well were cytotoxic neutrophils (Fig. 5a and Extended Data Fig. 6d) raising the possibility that neuropilin-1 may be a novel biomarker of anti-tumor neutrophils in BC – a hypothesis that remains to be functionally tested.

Nuclear expression of Sox9 has been associated with stemness in mammary tissue and mammary carcinoma[5,54,55]. We observed CC3 and nuclear Sox9 staining to be mutually exclusive (Fig. 5c and Extended Data Fig. 5b) at the *border* of cell death/neutrophil rich region providing direct *in vivo* evidence that the CSCs were resistant to the most potent tumor killing therapy in our screen. In contrast, galectin-3 and Sox9 were co-expressed in many areas of the *border* region (Fig. 5c, d) with 22% of galectin-3+ cells being CSCs (Fig. 5b). This indicates galectin-3 might be classified as a new biomarker enriching CSCs in breast cancer. Expression and spatial association of galectin-3 with both response (MHC-I, calreticulin) and resistance (PD-L1 and CSCs) mechanisms (Fig. 5a-d) suggest pleiotropic involvement of this protein which implies that targeting galectin-3 during immunogenic cell death should be carefully considered (Extended Data Fig. 6c).

Finally, we wanted to measure which immune cells are spatially located within the resistant cancer stem cell niche. Three spatial analyses, including macroscopic profile plots of relative cell abundance (Fig. 5a), as well as the distance-based cluster analyses (Fig. 5d), and pairwise proximity measurements in Sox9 microcultures (Fig. 5e, f and Extended Data Fig. 6e, f) showed that CD11c+ dendritic cells were preferentially located in close proximity to CSCs, suggesting functional interactions between the two cell types.

Combination of panobinostat, venetoclax and anti-CD40 immunotherapy maximizes tumor killing and anti-tumor immunity in mammary carcinoma

The observed spatial association between CSC and DC allowed us to generate a model of drug response maximizing anti-tumor activity through immune-modulation. In this model (Fig. 6a),

panobinostat induces immunogenic cell death of bulk tumor while CSCs remain resistant in the TME. Venetoclax induces recruitment of DCs that we have shown to localize to the – now accessible – CSC niche. We hypothesize that CD40 ligation induced licensing of DCs that had captured and processed antigen from neighboring CSCs, would result in activation of CSC-specific anti-tumor immunity leading to complete tumor clearance. Thus, panobinostat is presumed to induce antitumor immunity on the level of bulk tumor, while venetoclax/anti-CD40 may induce anti-tumor immunity on the level of resistant, tumor initiating cancer stem cells.

We tested the possibility that combination of panobinostat/venetoclax (PV) with anti-CD40 immunotherapy would provide maximal therapeutic efficacy in breast cancer. We tested this by systemically treating mice bearing EMT6 and E0771 tumors and compared the responses to those obtained using a PV/anti-PD-1 combination. Treatment with PV/anti-PD-1 significantly reduced the tumor burden as compared to dual PV and panobinostat/anti-PD-1 (Fig. 6b, c) treatments with survival rates of 40% in mice bearing EMT6 tumors (Fig. 6c). The triple combination of PV/anti-CD40, however, was superior and eliminated measurable tumors in 100% of EMT6 tumors and 85% of E0771 tumors, respectively (Fig. 6c, d). We also assessed the efficacy of PV/anti-CD40 against spontaneous tumors arising in the MMTV-PyMT model and found that this combination inhibited tumor progression and doubled the overall survival (Fig. 6d). Importantly, none of the combination treatments in whole animal studies were associated with adverse events, likely because we used lower systemic concentrations of drugs than published previously. While antigen specific T cell responses remain to be critically evaluated, overall, these results suggest the triple combination of panobinostat, venetoclax and anti-CD40 as a highly synergistic therapeutic strategy for long term breast cancer control.

Conclusion

The MIMA platform described here provides a strategy to design effective combination regimens based on intratumor nanodose exposure to a range of agents (Supplementary Table 4), coupled with highly multiplexed phenotyping and integrated spatial analysis of tumor response to each therapy. The focal drug delivery begins at the time of implantation and can be treated as a spatial and temporal pharmacological perturbation. Since distances from the drug delivery wells reflect recruitment events, analyses of the responses produced by devices left in place provide data about drug induced changes in cellular densities, molecular phenotypes and possible functional

cell interactions. These MIMA based observations rapidly translate into models of drug response in which we can identify therapeutic vulnerabilities that can be used to predict effective TME-modulating combination treatment strategies (Fig. 2f,g, 3f, g and 6a). Many of these drug effects are difficult or impossible to study in animal models treated systemically, due to heterogeneous and indeterminate drug distribution that can vary greatly over different regions of a tumor and over time. The TME response patterns obtained from MIMA studies may in future be used as early *in situ* biomarkers of therapeutic response and their further computational processing could provide actionable information to guide the development of effective drug doses and schedules.

By testing multiple therapeutic strategies in the same tumor, we can for the first time perform systems level analysis using multiple parallel pharmacological perturbations in the same organism. Furthermore, recent work by Jonas et al has demonstrated that IMD applications are safe and feasible in patients across multiple cancer indications including breast, prostate, T cell lymphoma and glioblastoma[27]. It may become feasible to use the MIMA approach to measure multiple drug responses in individual patients to guide their combination treatment design.

Although intended as proof of concept that analyses of local nanodose drug responses can effectively guide systemic treatment strategies, we have already identified specific therapeutic strategies that warrant clinical consideration. Based on local, significantly enriched histopathological signatures, we predicted synergies of palbociclib with anti-CSF1R, venetoclax with anti-CD40, panobinostat with anti-PD-1 monoclonal antibody and doxorubicin with vasculature-normalizing agents (not validated here). These strategies have been tested in only a few model systems and more extensive testing in subtype specific manner is warranted. However, the combination of lower dose panobinostat/venetoclax/anti-CD40 appears especially effective in three different models and so should be considered for clinical evaluation.

All in all, MIMA represents a new approach to identification of effective combination regimens for individual patients on a personalized basis. Extended use of MIMA will also open new opportunities in *in silico* modeling to model dynamic drug-tumor-stromal interactions.

Acknowledgements

We thank the OHSU Histopathology Share Resources core (Todd Camp, Joscelyn Zarceno and Cheyenne Martin) for careful FFPE processing of the MIMA tumor samples; Young Hwan

Chang, Sam Sivagnanam, Eugene Manley and AeSoon Bensen for help with image processing and mIHC/cycIF staining; Tiziana Cotechini for sharing the LPA3 mouse model line; and Marilyn McWilliams and Dottie Waddell breast cancer advocates for valuable feedback during project reports. This work was supported by the Susan G. Komen grant SAC190012 (JWG), the NIH/NCI Cancer Systems Biology Consortium Center U54CA209988 (JWG), and the NIH grant R01CA223150 (OJ, LMC).

Author contributions

Conceptualization, ZT, OJ, JWG; Methodology, ZT, OJ, JWG; Software, ZT, DCB; Investigation, ZT, DCB; Data Analysis and Interpretation, ZT, OJ, JWG; Writing – original and final draft, ZT, OJ, JWG; Writing – review & editing, JEK, LMH, JLM, PJS, SWA, GBM, LMC; Resources, JLM, LMC, OJ, JWG; Funding, OJ, JWG; Supervision, OJ, JWG.

Declaration of interests

J.E.K. is a cofounder and stock holder of Convergent Genomics.

GBM has licensed technologies to Myriad Genetics and Nanostring; is on the SAB or is a consultant to Amphista, AstraZeneca, Chrysallis Biotechnology, GSK, ImmunoMET, Ionis, Lilly, PDX Pharmaceuticals, Signalchem Lifesciences, Symphogen, Tarveda, Turbine, and Zentalis Pharmaceuticals; and has stock/options/financial interests in Catena Pharmaceuticals, ImmunoMet, SignalChem, and Tarveda.

LMC is a paid consultant for Cell Signaling Technologies, Shasqi Inc., and AbbVie Inc.; received reagent and/or research support from Janssen Research & Development, LLC, Abbott Labs, Eisai, Inc., ImClone, Aduro Biotech, Inc., Becton Dickinson, Plexxikon Inc., Pharmacyclics, Inc., Acerta Pharma, LLC, Deciphera Pharmaceuticals, LLC, Genentech, Inc., Roche Glycart AG, Syndax Pharmaceuticals Inc., Innate Pharma, and NanoString Technologies, and Cell Signaling Technologies; and is a member of the Scientific Advisory Boards of Syndax Pharmaceuticals, Carisma Therapeutics, Zymeworks, Inc, Verseau Therapeutics, Cytomix Therapeutics, Inc., and Kineta Inc., Hibercell, Inc., Cell Signaling Technologies, Alkermes, Inc.

O.J. is a consultant to Kibur Medical. Dr. Jonas's interests were reviewed and are managed by BWH and Mass General Brigham in accordance with their conflict of interest policies.

JWG has licensed technologies to Abbott Diagnostics, PDX Pharmaceuticals and Zorro Bio; has ownership positions in Convergent Genomics, Health Technology Innovations, Zorro Bio and PDX Pharmaceuticals; serves as a paid consultant to New Leaf Ventures; has received research support from Thermo Fisher Scientific (formerly FEI), Zeiss, Miltenyi Biotech, Quantitative Imaging, Health Technology Innovations and Micron Technologies; and owns stock in Abbott Diagnostics, AbbVie, Alphabet, Amazon, AMD, Amgen, Apple, Berkshire, Cisco systems, Clorox, Colgate Palmolive, Crown Castle Int., Humana, Keysight, Linde, Proctor and Gamble, Qualcomm, Unilever, Gilead, Intel, Johnson & Johnson, Microsoft, Nvidia, Taiwan Semiconductor, and Zimmer Biomet.

The other authors declare no competing interests.

Methods

Murine Models

Mice were purchased from The Jackson Laboratory. All animal studies were conducted in accordance with protocols approved by Institutional Animal Care and Use Committee (IACUC) at OHSU (protocol number: IP00000956). All mice were bred and housed under specific pathogen free conditions under a standard 12h light / 12h dark cycle. C57LB/6, BALB/c, and FVB/N mice were purchased from the Jackson Laboratory. MMTV-PyMT were from Dr. Lisa Coussens and purchased from the Jackson Laboratory. Virgin female mice of 8-24 weeks of age were used for all experiments.

Cell lines

EMT6 (mouse breast cancer) cells were purchased from American Type Culture Collection and were maintained in Waymouth's medium with 10% FBS, and 2mM L-glutamine. E0771 (mouse breast cancer) cells were purchased from CH3 BioSystems® and were cultured in RPMI-1640 with 10% FBS and 10mM HEPES. Both cell lines were pathogen tested and were grown at 5% CO_2 and 37C.

Experimental design

The objective of the studies in figures is to show how intact tumor microenvironment responds to local stimulus of drug release and to test whether this response was significantly different from the baseline tumor microenvironmental state in tumor region distant from the drug site. The number of independent biological replicates of each experiment (n) performed are given in the figure legends. Spatial systems analyses were designed to quantitatively define directional spatial cell dependencies and cause consequence cell association with distance from the reservoir translating to models of drug response. Within these models we aimed to identify therapeutic vulnerabilities to predict rational immune or TME modulating treatment combinations and their optimal schedule/sequencing which we then validated in traditional whole animal studies.

Microdevice implantation studies and sample collection

Nanodose drug delivery devices were manufactured and implanted as described previously in [25]. Briefly, cylindrical microdevices 5.5mm in length and 750μm in diameter were manufactured from medical-grade Delrin acetyl resin blocks (DuPont) by micromachining (CNC Micromachining Center) with 18 reservoirs 200μm (diameter) x 250μm (depth) on the outer surface. Reservoirs were packed with drugs mixed with Polyethylene glycol (PEG, MW 1450, Polysciences) polymer at the concentrations indicated in Table S1. Recommended systemic dose in cancer patients was derived from the https://rxlist.com web page to June 2017. Systemic doses ranging between 0-1mg/kg, 1-2mg/kg, 2-4mg/kg, >4mg/kg translate to 20%, 25%, 30% and 40% of drug concentration in PEG, respectively, when released from the nanowell. The calibration was determined previously using mass spectrometry measurements (Jonas et al., 2015). Pure PEG was used in control conditions. Implanting multiple devices per tumor and/or multifocal animal model can increase the throughput up to 50-70 times as compared to conventional systemic treatment studies. When two drugs were loaded into one reservoir, they were at approximately 1:1 ratio. The combination partner was loaded on the bottom of the well; panobinostat was released first. Microdevices were implanted for three days in MMTV-PyMT with late stage spontaneously growing tumors in all experiments. Tumor size was between 1.2 - 1.5cm in the longest dimension at the time of implant. Tumors were excised at three days after device implantation unless otherwise stated, fixed for 48h in 10% formalin or 4% paraformaldehyde, then perfused with paraffin. Specimen were sectioned using a standard microtome and 5μm tissue sections were collected from each reservoir. Dry FFPE tissues were

baked in a 65`C oven for 30mins. Following deparaffinization with xylene and rehydration in serially graded alcohol to distilled water, slides were subjected to endogenous peroxidase blocking in fresh 3% H_2O_2 for 10 minutes at RT. Sections were then stained by multiplex immunohistochemistry and/or cyclic immunofluorescence (see also Extended Data Fig. 2b and c).

Cyclic Immunofluorescence

Before iterative cycles of (i) staining, (ii) whole slide scanning and (iii) fluorophore bleaching, the slides were subjected to heat-mediated antigen retrieval immersed in citrate buffer (pH 5.5, HK0809K, BioGenex Laboratories Citra Plus Antigen Retrieval), then in Tris/EDTA buffer (pH 9.0, S2368, Dako Target Retrieval Solution) using Cuisinart Electric Pressure Cooker (CPC-600N1) for total of 35 to 40 minutes. Protein blocking was performed for 30 minutes RT with 10% normal goat serum (S-1000, Vector Lab) and 1% bovine serum albumin (BP1600-100) in 1xPBS. (i) Slides were incubated with primary antibody (concentrations defined in Table S2) for 2 hours at RT while being protected from light in a dark humid chamber. All washing steps were performed for 3 x 2-5 minutes in 1xPBS while agitating. Slides were mounted with SlowFade Gold antifade mountant with DAPI (S36938) using a Corning Cover Glass (2980-245). (ii) Images were acquired using Zeiss Axio Scan.Z1 Digital Slide Scanner (Carl Zeiss Microscopy) at 20x magnification after which the coverslips were gently removed in 1xPBS while agitating. (iii) Fluorophores were chemically inactivated using a 3% H_2O_2 and 20mM NaOH in 1xPBS for 30 minutes at RT while being continuously illuminated. The fluorophore inactivation was repeated twice with a short, 10-minute, 1xPBS wash in between. Efficacy of bleaching was imaged before antibody incubation (baseline autofluorescence) and every third to fourth cycle in average. After protein blocking, samples were subjected to the next round of staining. Single cell feature extraction was not applied to evaluate sections stained by cyclic immunofluorescence.

Multiplex Immunohistochemistry

Before iterative cycles of (i) staining, (ii) whole slide scanning and (iii) and heat and chemical stripping of antibodies and chromogen, the slides were subjected to staining with F4/80 and CSF1R antibodies (cycle zero, no antigen retrieval, Supplementary Table 2) and hematoxylin staining (S3301, Dako) for 1-5mins followed by whole slide scanning. Slides were then

subjected to the first heat-mediated antigen retrieval in 1x pH 5.5-6 citrate buffer (Biogenex Laboratories, HK0809K) for 90 seconds in a low power microwave and 16 minutes in a steamer followed by protein blocking with 10% normal goat serum (S-1000, Vector Lab) and 1% bovine serum albumin (BP1600-100) in 1xPBS for 30 minutes RT. (i) Slides were incubated with primary antibodies (concentrations defined in Table S2) for 1 hour at RT or 16-17 hours at 4 degrees Celsius while being protected from light in a dark humid chamber. Signal was visualized with either anti-rabbit or anti-rat Histofine Simple Stain MAX PO horseradish peroxidase (HRP) conjugated polymer (Nichirei Biosciences) followed by peroxidase detection with 3-amino-9-ethylcarbazole (AEC). Two or three drops of HRP polymer were used for up to nickel-size or whole slide tissue sample, respectively. Timing of AEC development was determined by visual inspection of positive control tissue (Extended Data Fig. 1d-f) for each antibody. All washing steps were performed for 3 x 5-10 minutes in 1xPBS while agitating. Slides were mounted with a filtered 1xPBS with 0.075% Tween20 (BP337100) using a Signature Series Cover Glass cover glass (Thermo Scientific, 12460S). (ii) Images were acquired using the Aperio ImageScope AT (Leica Biosystems) at 20x magnification after which the coverslips were gently removed in 1xPBS while agitating. (iii) Within one cycle, removal of AEC and HRP inactivation was accomplished by incubating the slides in 0.6% fresh H_2O_2 in methanol for 15 minutes; AEC removal and stripping of antibodies was accomplished by Ethanol gradient incubation and heat-mediated antigen retrieval such as described above between cycles. After washing and protein blocking, samples were subjected to the next round of staining.

Image processing and feature extraction of mIHC images

The iteratively digitized images were co-registered using Matlab (The MathWorks, Inc., Natic, MA, version 2019b) utilizing the detectSURFFeatures algorithm from the Computer Vision Toolbox. The imperfectly registered images were additionally processed using the Linear Stack Alignment with SIFT plugin (Fiji) so that cell features overlap down to a single pixel level. Hematoxylin-stained images were color deconvoluted for single cell nuclear segmentation to generate a binary mask using watershed function and standard image processing steps (noise removal, erosion, dilation; Fiji) [57]. AEC chromogenic signal was extracted using the NIH plugin RGB_to_CMYK to separate AEC signal into the yellow channel for improved sensitivity of IHC evaluation [58,59]. Gray scale images of all proteins and the binary mask were imported to

CellProfiler (version 3.1.8, Broad Institute) [60] to quantify single cell signal mean intensity as defined by mask which was scaled to a range 0-1. IdentifyPrimaryObjects module was used to identify nuclei from mask; MeasureObjectIntensity module measured mean intensity for each object for each protein. The mean signal intensity per cell output was imported to FCS Express 6 and 7 Image Cytometry Software (DeNovo Software) to perform multidimensionality reduction to classify "cell standards". Gating strategies and hierarchical cell classification is presented in Fig. 1e and Extended Data Fig. 2e. Polygonal gates moving around central vertex without changing the polygon shapes was used to obtain quantitatively reproducible multiplex data, batch to batch, independent of the condition measured. Positive control tissues were used to help to define single parameter threshold for positivity by manual gating. Total of 3000-5000 cells were analyzed for feature extraction in the assay area located above the drug releasing site with ± 300 total cells for paired, experimental vs control, region. Minimum population proportion within 5% margin of error and 95% confidence level was set to 0.75% (represents 12 cells) to discriminate noise from specific cell enrichment induced by e.g. increased protein expression or cell recruitment into the assay region. Experimental condition of the assay area was compared to random control intratumoral region located perpendicular and/or far from the drug-releasing reservoir. To obtain greater control over cofounding variables, paired sample one tailed t-tests were used to determine enrichment of induced TME states. Percentage of positivity and significance was presented in form of a heatmap or bar graphs. Quality of the single cell data was ensured by excluding deformed (folded), lost or unevenly stained tissue (border effects). The assay area was determined by the first 3000-5000 cells above the well excluding these deformed regions. Single cell data from FCS Express was extracted in data grid to Matlab for downstream spatial systems analyses. In computed images, neutrophils are presented independent of the Epcam± status.

Spatial Systems Analyses

Distance based cluster function finds clusters in a set of spatial points expressed in XY space (adapted and modified from Yann Marcon; Matlab October 2019). The clustering is based on Euclidean distance between the points (cells). The function does not require the number of clusters to be known beforehand. Each cell clusters with the closest neighboring cell if distance between the two cells is shorter than the defined threshold. Minimal number of cells per cluster

are defined by user. The function outputs non-clustering cells in gray color while each cluster meeting the defined parameters (minimal number of cells within maximum distance range) are presented in randomized colors. Clusters within the maximum defined distance merge and share one color. Number of clusters and total coverage in the assay area was calculated using distinct cluster sizes (defined by minimal number of cells within maximum distance range) for control PEG and palbociclib which identified that cells cluster in response to treatment if minimum 10 cells are present within maximum distance rage 30-75µm (systematic comparison not shown in this study). Cluster parametrization using as few as 5 cells and distances as large as 100µm resulted in treatment non-specific cluster formation in PEG negative control. Treatment specific cluster formation with cluster definition of minimum 10 cells within 50µm distance was generalizable to all marker and standard cell types which was confirmed in panobinostat condition by comparing assay area and distal region side by side in one field of view (Extended Data Fig. 6e). This treatment specific cluster parametrization was applied in downstream analytics to identify hotspots/zones of interest (e.g. *proximal*, *border*, *distal*, network adjacent, CD11c+ DC clusters) in an objective, biology driven, manner.

For the relative abundance profile plot, marker positive cells and the standard cell types were extracted to XY coordinate space, signal was blurred using Gaussian Blur filter and relative abundance of positive cells was displayed with distance from the well in a profile plot as outlines in corresponding Extended Data Figures. A moving average filter with 50µm; and 100µm window size (movmean function; Matlab) was additionally applied to smoothen the feature signal for palbociclib and panobinostat condition, respectively. Signal in the profile plots was not scaled.

Inside the hotspot, spatial (geographical) interactions between marker positive cells were determined by proximity measurements in local microculture by using the pdist2 function in Matlab (MathWorks, Inc., Natic, MA, version 2019b) which returns the distance of each pair of observations (positive cells) in X and Y using metric specified by Euclidean distance. Random circular regions of 175μm diameter (defined by Extended Data Fig. 6f) were selected in the border, cancer stem cell, zone of the panobinostat assay area and Euclidean distance was measured between Sox9+ and other marker positive cells. The number of distances was presented in form of a histogram. To quantify spatially interrelated phenomenon, proportions of

distances lower than 50µm (as defined by distance-based cluster analyses) was compared between different cell pairs (e.g. Sox9+/Ly6G+ vs Sox9+/CD11c+).

Extended hierarchical cell classification was applied to characterize the significantly enriched cell phenotypes forming zones of interest which were outside the standard cell type classification (e.g less differentiated macrophages or phagocytic DCs). Probe combination, number of cells analyzed within number of clusters are defined in the figures and figure legends.

2D composite and 3D composite images were presented by using Fiji [57] and QiTissue Quantitative Imaging System (http://www.qi-tissue.com).

The spatial systems analyses were used to identify drug models of response (presented as line diagrams) and the identified therapeutic vulnerabilities were tested in whole animal studies.

Whole animal treatment studies

While the high-throughput IMD experiments were perfomed in the MMTV-PyMT model[31,32,61,62] with spontanously growing tumors; the whole animal validation studies of predicted immune-modulating combinations were perfomed using transplantable breast cancer cell lines in syngeneic mice to avoid extensive breeding and colony maintenance necessary to test synergy of multiple predicted combinations. E0771 and EMT6 models, which are typically used in breast cancer research involving immunotherapy testing[63–65], were selected randomly for validation of different combinatios. The combination of panobinostat and anti-PD-1 was tested in both transplantable models. The most potent triple combination of panobinostat, venetoclax and anti-CD40 was additionally tested in the MMTV-PyMT model with spontanously growing tumors.

MMTV-PyMT transgenic mice that were 80 days old were randomized and included in the study when their total tumor burden was between 150-550mm^3 (treatment initiation). For the orthotopically induced tumor models of mammary carcinoma, EMT6 (0.5 x 10^6 in 1xPBS per site), E0771 (0.5 x 10^6 in Corning matrigel per site) and primary tumor derived LPA3 (0.8 x 10^5 in Corning matrigel per site) cells were injected into the #4 mammary fat pad of female virgin C57LB/6, BALB/c, and FVB/N mice, respectively. One tumor was induced in the E0771, LPA3 models and two tumors were induced in the EMT6 model. Caliper measurements were used to calculate the tumor volumes using formula length x width^2 / 2. Treatments were initiated when total tumor burden was between 60-150mm^3. For all models, the endpoint was determined by

tumor volume above 2000mm^3 in two consecutive measurements or one measurement above 2200mm^3. Treatments were administered by intraperitoneal injection. Dose, schedule and duration are indicated in the respective figures and figure legends. Treatment schedule was estimated depending on the location of the targetable cell phenotype in proximity to the well or more distal from the drug source. E.g. cells in the *immediate proximity* to the drug well at 3 days of exposure were likely recruited first to the drug assay area thus early targeting (pre-treatment) of these cells is preferred. Inversely, cells located in *distal* regions should be targeted by posttreatment approach. Diluent and IgG2a isotype control (BioXCell) concentrations were equivalent to the highest dose of the respective drug used in each experiment.

The mice were monitored daily to determine any possible effects on the general condition of the animals using parameters as established by (Morton and Griffiths, 1985). The guidelines for pain, discomfort and distress recognition were used to evaluate weight loss, appearance, spontaneous behavior, behavior in response to manipulation and vital signs. Specifically, general appearance (dehydration, missing anatomy, abnormal posture, swelling, tissue masses, prolapse) skin and fur appearance (discoloration, urine stain, pallor, redness, cyanosis, icterus, wound, sore, abscess, ulcer, alopecia, ruffled fur), eyes (exophthalmos, microphthalmia, ptosis, reddened eye, lacrimation, discharge, opacity), feces (discoloration, blood in the feces, softness/diarrhea), locomotor (hyperactivity, coma, ataxia, circling) were monitored to determine loss of body condition (BC) score, namely: BC 1 (emaciated) score applied when skeletal structure was extremely prominent with little or no flesh/muscle mass and vertebrae was distinctly segmented; BC 2 (under-conditioned) score applied when segmentation of vertebrate column was evident, dorsal pelvic bones were readily palpable and muscle mass was reduced; BC 3 (well-conditioned) applies when vertebrae and dorsal pelvis were not prominent/visible, and were palpable with slight pressure. Loss of BC was also considered when anorexia (lack or loss of appetite) or failure to drink; debilitating diarrhea, dehydration/reduced skin turgor; edema, sizable abdominal enlargement or ascites, progressive dermatitis, rough hair coat/unkempt appearance, hunched posture, lethargy, loss of righting reflex, neurological signs or bleeding from any orifice appeared in treated mice. Majority of treated groups were well-conditioned (BC score 3); less than 20% of mice in each group experienced mild diarrhea for up to 2 days once during the course of treatment (typically post first or second therapy administration). Mice receiving palbociclib monotherapy were under-conditioned (BC score 2) starting from day 3 till

the end of the treatment. Two out of eight mice in the MMTV-PyMT model died within 1-3 days after first injection of αCD40 immunotherapy when administered as single agent. Lethal toxicity of anti-CD40 used as a single agent was previously reported due to a shock-like syndrome [66] and our data also strongly suggest this immunotherapy is tolerable only with prior administration of anti-cancer agent(s). Surviving mice receiving venetoclax/anti-CD40 combination experienced fur graying to different degree starting approximately four weeks post treatment. No signs of pain, discomfort or distress were observed in the surviving mice. Emaciated (BC score 1), over-conditioned (BC score 4) nor obese (BC score 5) were observed in our studies.

To show CD8+ T cell infiltration inside the tumor bed, ErbB2ΔEx16 mice[67] with spontaneously growing late stage tumors were intraperitoneally injected with panobinostat (15mg/mg) on day 0, 2 and 4. Tumors were extracted at day 7, were FFPE processed and were stained for CD8 to compare the rate of intratumoral CD8+ T cells in panobinostat treated vs control (diluent) treated mice.

Vaccination study

EMT6 and E0771 cells in tissue culture were treated with a soluble drug panobinostat at 5μM concentration when they would reach 60-70% confluency. After two days the cells were harvested and were injected subcutaneously (total 2-3 x 10^6 cells) into lower left flank of BALB/c and C57Bl6 mice, respectively. Cells freeze-thawed three times served as negative control for non-immunogenic form of cell death. After 7-8 days, the mice were re-inoculated by injecting living cells orthotopically into one #4 mammary fat pad (total 0.5 x 10^6 cells) and tumor appearance was monitored by minimal tumor size approximately 5mm and 3.5mm in the longest dimension for E0771 and EMT6 model, respectively (palpable tumors). We note the E0771 tumors after re-challenge appeared at the primary subcutaneous site and no tumors were developed in the orthotopic site.

Statistical analysis

All data are combined from two to three independent experiments, unless specifically noted. To accomplish randomization for systemic mouse experiments, animals were sorted by a blinded investigator and then groups were assigned. Each group was checked post-hoc to verify no statistical significance in average starting tumor size. There was no sample-size estimation of in

667 standard drug treatment experiments. Data are shown as mean ± SEM, unless otherwise noted.
668 For tumor growth rate, significance was calculated by unpaired two-tailed t-test with equal
669 variance. For survival and tumor free analyses, Kaplan-Meier curves were generated to
670 demonstrate time to event and log-rank (Mantel-Cox) test was used to evaluate statistical
671 significance.
672
673 **References**

674 1. Letai, A. Functional precision cancer medicine-moving beyond pure genomics. *Nat. Med.*
675 **23**, 1028–1035 (2017).

676 2. Li, A. *et al.* Characterizing advanced breast cancer heterogeneity and treatment resistance
677 through serial biopsies and comprehensive analytics. *npj Precis. Oncol.* **5**, (2021).

678 3. Hanker, A. B., Sudhan, D. R. & Arteaga, C. L. Overcoming Endocrine Resistance in
679 Breast Cancer. *Cancer Cell* **37**, 496–513 (2020).

680 4. Brady, S. W. *et al.* Combating subclonal evolution of resistant cancer phenotypes. *Nat.*
681 *Commun.* (2017) doi:10.1038/s41467-017-01174-3.

682 5. Jeselsohn, R. *et al.* Embryonic transcription factor SOX9 drives breast cancer endocrine
683 resistance. *Proc. Natl. Acad. Sci. U. S. A.* **114**, E4482–E4491 (2017).

684 6. Kowal, J., Kornete, M. & Joyce, J. A. Re-education of macrophages as a therapeutic
685 strategy in cancer. *Immunotherapy* **11**, 677–689 (2019).

686 7. Robert, C. A decade of immune-checkpoint inhibitors in cancer therapy. *Nat. Commun.*
687 **11**, 10–12 (2020).

688 8. Adams, S. *et al.* Current Landscape of Immunotherapy in Breast Cancer: A Review.
689 *JAMA Oncol.* **5**, 1205–1214 (2019).

690 9. Force, J., Leal, J. H. S. & McArthur, H. L. Checkpoint Blockade Strategies in the
691 Treatment of Breast Cancer: Where We Are and Where We Are Heading. *Curr. Treat.*
692 *Options Oncol.* **20**, (2019).

693 10. Hugo, W. *et al.* Genomic and Transcriptomic Features of Response to Anti-PD-1 Therapy
694 in Metastatic Melanoma. *Cell* **165**, 35–44 (2016).

11. Lee, H. J. *et al.* Differential expression of major histocompatibility complex class I in subtypes of breast cancer is associated with estrogen receptor and interferon signaling. *Oncotarget* **7**, 30119–30132 (2016).

12. Inoue, M. *et al.* Expression of mhc class i on breast cancer cells correlates inversely with her2 expression. *Oncoimmunology* **1**, 1104–1110 (2012).

13. Janiszewska, M. *et al.* The impact of tumor epithelial and microenvironmental heterogeneity on treatment responses in HER2+ breast cancer. *JCI Insight* **6**, (2021).

14. Denardo, D. G. *et al.* Functionally Regulates Response to Chemotherapy. *Cancer Discov.* 54–67 (2011) doi:10.1158/2159-8274.CD-10-0028.Leukocyte.

15. Gil Del Alcazar, C. R. *et al.* Immune escape in breast cancer during in situ to invasive carcinoma transition. *Cancer Discov.* **7**, 1098–1115 (2017).

16. Palucka, A. K. & Coussens, L. M. The Basis of Oncoimmunology. *Cell* **164**, 1233–1247 (2016).

17. Galluzzi, L. *et al.* Molecular mechanisms of cell death: Recommendations of the Nomenclature Committee on Cell Death 2018. *Cell Death Differ.* **25**, 486–541 (2018).

18. Yatim, N., Cullen, S. & Albert, M. L. Dying cells actively regulate adaptive immune responses. *Nat. Rev. Immunol.* **17**, 262–275 (2017).

19. Abrams, J. *et al.* National Cancer Institute's Precision Medicine Initiatives for the New National Clinical Trials Network. *Am. Soc. Clin. Oncol. Educ. B.* 71–76 (2014) doi:10.14694/edbook_am.2014.34.71.

20. Hutter, C. & Zenklusen, J. C. The Cancer Genome Atlas: Creating Lasting Value beyond Its Data. *Cell* **173**, 283–285 (2018).

21. Rozenblatt-Rosen, O. *et al.* The Human Tumor Atlas Network: Charting Tumor Transitions across Space and Time at Single-Cell Resolution. *Cell* **181**, 236–249 (2020).

22. Jenkins, R. W. *et al.* Ex Vivo Profi ling of PD-1 Blockade Using Organotypic Tumor Spheroids. (2017) doi:10.1158/2159-8290.CD-17-0833.

23. Tatárová, Z., Abbuehl, J. P., Maerkl, S. & Huelsken, J. Microfluidic co-culture platform to quantify chemotaxis of primary stem cells. *Lab Chip* 1–8 (2016)

doi:10.1039/C6LC00236F.

24. Yuki, K., Cheng, N., Nakano, M. & Kuo, C. J. Organoid Models of Tumor Immunology. *Trends Immunol.* **41**, 652–664 (2020).

25. Jonas, O. *et al.* An implantable microdevice to perform high-throughput in vivo drug sensitivity testing in tumors. *Sci. Transl. Med.* **7**, 284ra57 (2015).

26. Watson, S. S. *et al.* Microenvironment-Mediated Mechanisms of Resistance to HER2 Inhibitors Differ between HER2 + Breast Cancer Subtypes Article Microenvironment-Mediated Mechanisms of Resistance to HER2 Inhibitors Differ between HER2 + Breast Cancer Subtypes. *Cell Syst.* 1–14 (2018) doi:10.1016/j.cels.2018.02.001.

27. Dominas, C. *et al.* The translational and regulatory development of an implantable microdevice for multiple drug sensitivity measurements in cancer patients. 1–10 (2021) doi:10.1109/TBME.2021.3096126.

28. Lin, J.-R., Fallahi-Sichani, M. & Sorger, P. K. Highly multiplexed imaging of single cells using a high-throughput cyclic immunofluorescence method. *Nat. Commun.* **6**, 8390 (2015).

29. Tsujikawa, T. *et al.* Quantitative Multiplex Immunohistochemistry Reveals Myeloid-Inflamed Tumor-Immune Complexity Associated with Poor Prognosis. *Cell Rep.* **19**, 203–217 (2017).

30. Kumar, N., Mb, T. & Dhesy-Thind Md Msc, S. CLINICAL PRACTICE GUIDELINES IN BREAST CANCER, Kumar Tyagi and Dhesy-Thind Clinical practice guidelines in breast cancer ABSTRACT Background A number of clinical practice guidelines (cpgs) concerning breast cancer (bca) screening and. *Curr. Oncol.* **25**, 151–160 (2018).

31. Guy, C. T., Cardiff, R. D. & Muller, W. J. Induction of mammary tumors by expression of polyomavirus middle T oncogene: a transgenic mouse model for metastatic disease. *Mol. Cell. Biol.* **12**, 954–961 (1992).

32. Lin, E. Y. *et al.* Progression to malignancy in the polyoma middle T oncoprotein mouse breast cancer model provides a reliable model for human diseases.Lin, E. Y., Jones, J. G., Li, P., Zhu, L., Whitney, K. D., Muller, W. J., & Pollard, J. W. (2003). Progression to malignan. *Am. J. Pathol.* **163**, 2113–26 (2003).

33. Hanahan, D. & Coussens, L. M. Accessories to the Crime: Functions of Cells Recruited to the Tumor Microenvironment. *Cancer Cell* **21**, 309–322 (2012).

34. Dunn, G. P., Old, L. J. & Schreiber, R. D. The Three Es of Cancer Immunoediting. *Annu. Rev. Immunol.* **22**, 329–360 (2004).

35. Mpekris, F. *et al.* Combining microenvironment normalization strategies to improve cancer immunotherapy. *Proc. Natl. Acad. Sci. U. S. A.* **117**, 3728–3737 (2020).

36. Bergers, G. & Song, S. The role of pericytes in blood-vessel formation and maintenance. *Neuro. Oncol.* **7**, 452–464 (2005).

37. Deszo, E. L., Brake, D. K., Cengel, K. A., Kelley, K. W. & Freund, G. G. CD45 Negatively Regulates Monocytic Cell Differentiation by Inhibiting Phorbol 12-Myristate 13-Acetate-dependent Activation and Tyrosine Phosphorylation of Protein Kinase Cδ. *J. Biol. Chem.* **276**, 10212–10217 (2001).

38. Norazmi, M. N., Hohmann, A. W., Skinner, J. M. & Bradley, J. Expression of MHC class II, interleukin 2 receptor and CD45 antigens on tumour-associated t lymphocytes in colonic carcinoma. *Br. J. Cancer* **60**, 685–687 (1989).

39. Domogalla, M. P., Rostan, P. V., Raker, V. K. & Steinbrink, K. Tolerance through education: How tolerogenic dendritic cells shape immunity. *Front. Immunol.* **8**, 1–14 (2017).

40. Goodridge, H. S. *et al.* Activation of the innate immune receptor Dectin-1 upon formation of a “phagocytic synapse". *Nature* **472**, 471–475 (2011).

41. Reis E Sousa, C. Dendritic cells in a mature age. *Nat. Rev. Immunol.* **6**, 476–483 (2006).

42. Griffiths, K. L. *et al.* Targeting dendritic cells to accelerate T-cell activation overcomes a bottleneck in tuberculosis vaccine efficacy. *Nat. Commun.* **7**, 1–13 (2016).

43. Sotomayor, E. M. *et al.* Conversion of tumor-specific CD4+ T-cell tolerance to T-cell priming through in vivo ligation of cd40. *Nat. Med.* **5**, 780–787 (1999).

44. Garg, A. D. *et al.* Pathogen response-like recruitment and activation of neutrophils by sterile immunogenic dying cells drives neutrophil-mediated residual cell killing. *Cell Death Differ.* **24**, 832–843 (2017).

45. Md Sakib Hossain, D. *et al.* Dinaciclib induces immunogenic cell death and enhances anti- PD1–mediated tumor suppression. *J. Clin. Invest.* **128**, 644–654 (2018).

46. Gittens, B. R., Bodkin, J. V, Nourshargh, S., Perretti, M. & Cooper, D. Galectin-3: A Positive Regulator of Leukocyte Recruitment in the Inflamed Microcirculation. (2018) doi:10.4049/jimmunol.1600709.

47. Patnaik, A. *et al.* Cabozantinib eradicates advanced murine prostate cancer by activating antitumor innate immunity. *Cancer Discov.* **7**, 750–765 (2017).

48. Obeid, M. *et al.* Calreticulin exposure dictates the immunogenicity of cancer cell death. *Nat. Med.* **13**, 54–61 (2007).

49. Aguilera, T. A. *et al.* Reprogramming the immunological microenvironment through radiation and targeting Axl. *Nat. Commun. Publ. online 23 December 2016;* | *doi10.1038/ncomms13898* **7**, 1974–1982 (2016).

50. Luo, N. *et al.* DNA methyltransferase inhibition upregulates responses in breast cancer. *Nat. Commun.* 1–11 (2018) doi:10.1038/s41467-017-02630-w.

51. Guerriero, J. L. *et al.* Class IIa HDAC inhibition reduces breast tumours and metastases through anti-tumour macrophages. *Nature* (2017) doi:10.1038/nature21409.

52. Chawla, A. *et al.* Neutrophil elastase enhances antigen presentation by upregulating human leukocyte antigen class I expression on tumor cells. *Cancer Immunol. Immunother.* **65**, 741–751 (2016).

53. Kerros, C. *et al.* Neuropilin-1 mediates neutrophil elastase uptake and cross-presentation in breast cancer cells. *J. Biol. Chem.* **292**, 10295–10305 (2017).

54. Guo, W. *et al.* Slug and Sox9 cooperatively determine the mammary stem cell state. *Cell* **148**, 1015–1028 (2012).

55. Xue, Y. *et al.* SOX9/FXYD3/Src Axis Is Critical for ER + Breast Cancer Stem Cell Function . *Mol. Cancer Res.* **17**, 238–249 (2019).

56. Fridlender, Z. G. *et al.* Polarization of Tumor-Associated Neutrophil Phenotype by TGF-β: 'N1' versus 'N2' TAN. *Cancer Cell* **16**, 183–194 (2009).

57. Schneider, C. a, Rasband, W. S. & Eliceiri, K. W. NIH Image to ImageJ: 25 years of

image analysis. *Nat. Methods* **9**, 671–675 (2012).

58. Pham, N. A. *et al.* Quantitative image analysis of immunohistochemical stains using a CMYK color model. *Diagn. Pathol.* **2**, 1–10 (2007).

59. Banik, G. *et al.* HHS Public Access. 1–20 (2020) doi:10.1016/bs.mie.2019.05.039.High-dimensional.

60. Carpenter, A. E. *et al.* CellProfiler: Image analysis software for identifying and quantifying cell phenotypes. *Genome Biol.* **7**, (2006).

61. Attalla, S., Taifour, T., Bui, T. & Muller, W. Insights from transgenic mouse models of PyMT-induced breast cancer: recapitulating human breast cancer progression in vivo. *Oncogene* **40**, 475–491 (2021).

62. Varticovski, L. *et al.* Accelerated preclinical testing using transplanted tumors from genetically engineered mouse breast cancer models. *Clin. Cancer Res.* **13**, 2168–2177 (2007).

63. Ewens, A., Mihich, E. & Ehrke, M. J. Distant metastasis from subcutaneously grown E0771 medullary breast adenocarcinoma. *Anticancer Res.* **25**, 3905–3915 (2005).

64. Rockwell, S. In vivo-in vitro tumour cell lines: characteristics and limitations as models for human cancer. *Br. J. Cancer. Suppl.* **4**, 118–122 (1980).

65. Herschkowitz, J. I. *et al.* Identification of conserved gene expression features between murine mammary carcinoma models and human breast tumors. *Genome Biol.* **8**, 1–17 (2007).

66. Van Mierlo, G. J. D. *et al.* CD40 stimulation leads to effective therapy of CD40- tumors through induction of strong systemic cytotoxic T lymphocyte immunity. *Proc. Natl. Acad. Sci. U. S. A.* **99**, 5561–5566 (2002).

67. Turpin, J. *et al.* The ErbB2ΔEx16 splice variant is a major oncogenic driver in breast cancer that promotes a pro-metastatic tumor microenvironment. *Oncogene* 1–12 (2016) doi:10.1038/onc.2016.129.

Fig. 1

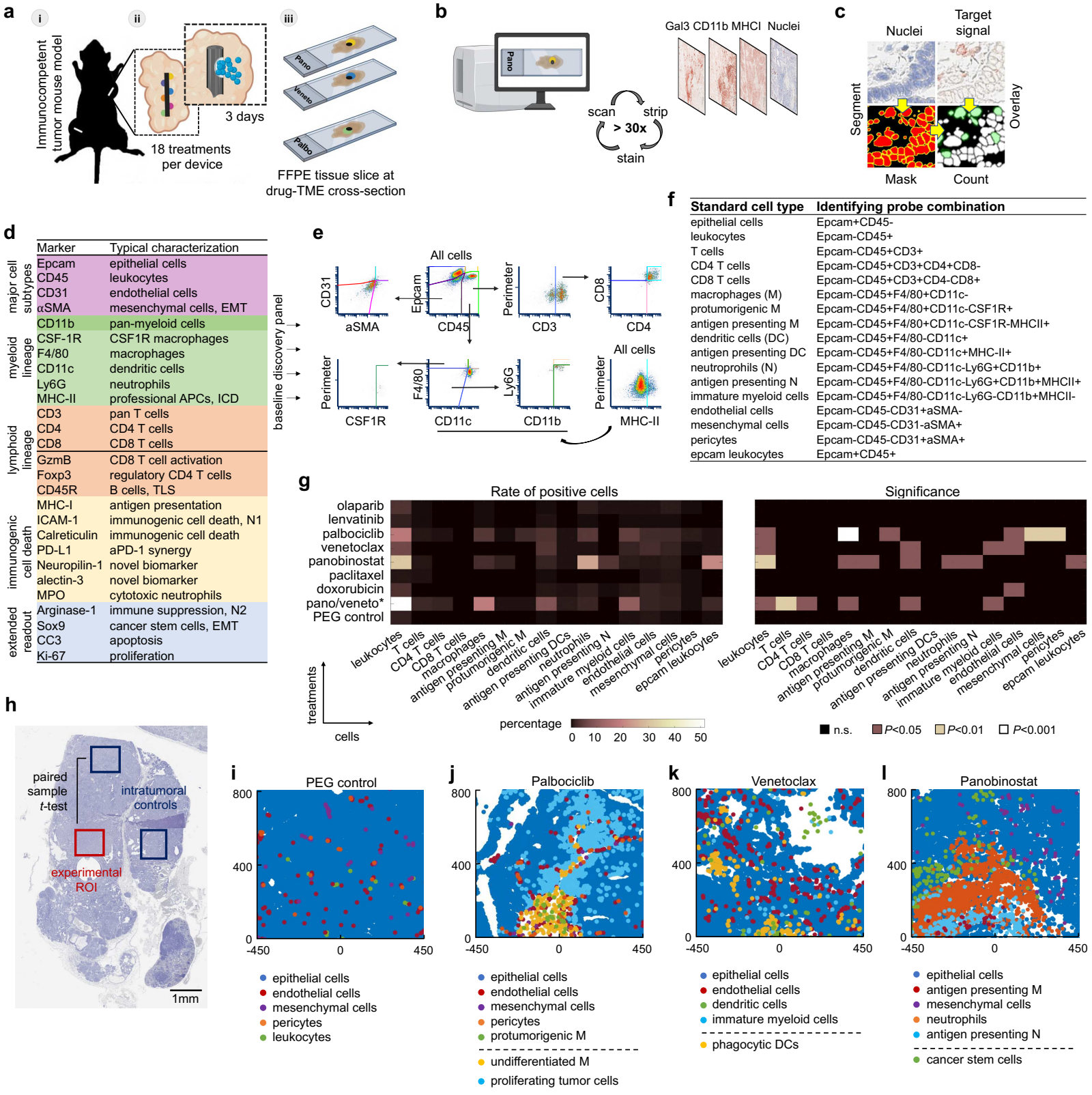

Fig. 1| MIMA components and testing of locally induced drug effects on TME. a, Schematic of IMDs implanted into a multifocal mouse model of mammary carcinoma (i) showing treatments being released into spatially separated regions of tumors through passive diffusion (ii) and each condition being assayed individually (iii). **b,** Schematic of the mIHC technique composed of iterative histological stripping, staining and scanning using digital scanning microscopy to detect the target set of markers. **c,** Acquired images are co-registered with nuclear staining and the mean intensity of antibody staining within a mask is calculated for each cell to count marker positive cells in a spatially intact tissue. **d,** Antibody list primary probe classification used to interrogate a broad range of tumor intrinsic and tumor-microenvironmental states. **e, f,** Multidimensionality reduction in hierarchical gating (e) and list of probe combinations identifying standard cell types (f). **g, h,** Heatmap of mean percentage of positive cells (left) and level of significance (right) at depicted targeted agents and chemotherapies (y-axis) with PEG being the negative control (g). Total cell counts were between 3000 to 5000 cells per assay area and were matched ± 300 total cells for paired samples: experimental vs control region as shown in the macroscopic view of the hematoxylin-stained tumor tissue implanted with IMD (h). Minimum population proportion within 5% margin of error and 95% confidence level was set to 0.75% (represents 12 cells) to discriminate noise from specific signal. n=3 wells from 3 tumors from 2-3 mice per treatment. MMTV-PyMT mice with late stage spontaneously growing tumors were implanted for three days. **i-l,** Presentation of selected standard cell types in XY space. [0,0] coordinate is the drug releasing site; direction of release is upward.

Fig. 2

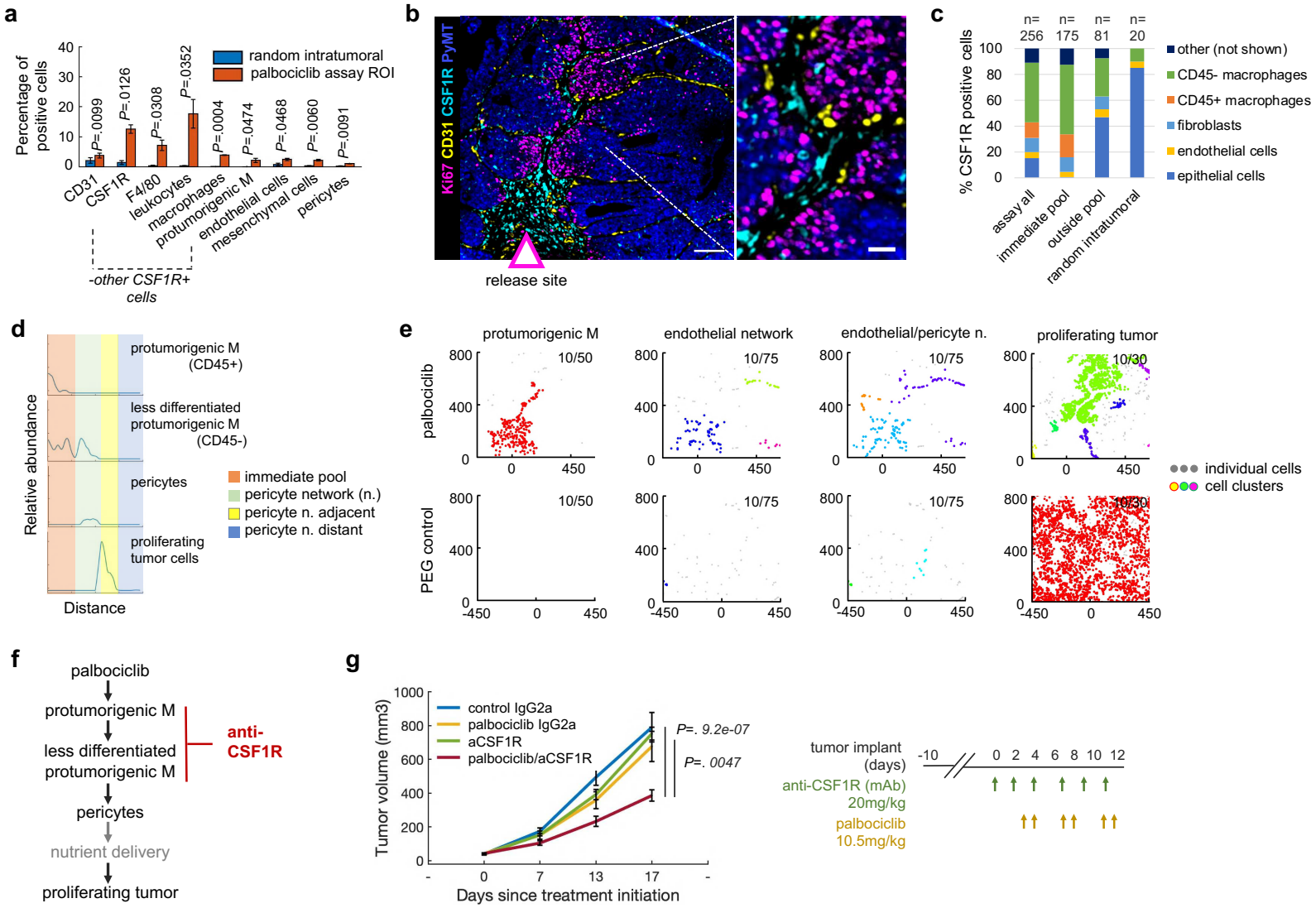

Fig. 2| Local TME changes induced by palbociclib and whole animal studies testing the combination efficacy with predicted anti-CSF1R immunotherapy. a, Quantification of single cell events using individual markers and standard cell type classification. Bars are mean ± s.e.; n=3 reservoirs. Significance was calculated by paired sample one tailed t-test. For quantification of all TME lineages, see Extended Data Fig. 4a.. **b,** Sample composite image of the key response markers at the palbociclib well. Scale bar is 100μm (left); and 25μm (right). **c,** Percentage of top five cell types expressing CSF1R stratified by zones in the palbociclib assay area. "Immediate pool" zone is visualized by the dashed line in Extended Data Fig. 4c. The number of cells analyzed (n) is shown. **d,** Line profile of relative cell abundance as a function of distance from well (left to right). Assay zones are color-coded in the legend; profile line is shown in Extended Data Fig. 4c.. **e,** Distance-based clustering of depicted cell types as a set of XY coordinates. Coordinate [0,0] identifies the drug source. The direction of the drug release is upward. Clusters were identified by a minimum 10 cells within maximum distances of 50μm, 75μm and 30μm for CSF1R+ protumorigenic macrophages, endothelial/pericyte network and proliferating tumor cells, respectively. Each cluster is depicted with a randomized color; individual (non-clustering) cells are shown as light gray points. **f,** Palbociclib model of response presented as line diagram and site of intervention using immunotherapy depicted in red. **g,** Tumor burden measurement of mice bearing EMT6 tumors after systemic treatment using drugs as color-coded in the graph. Shown is mean ± s.e.; n=8 to 10 tumors per group. Significance was calculated using an independent two-sample two-tailed t-test with equal variance.

Fig. 3

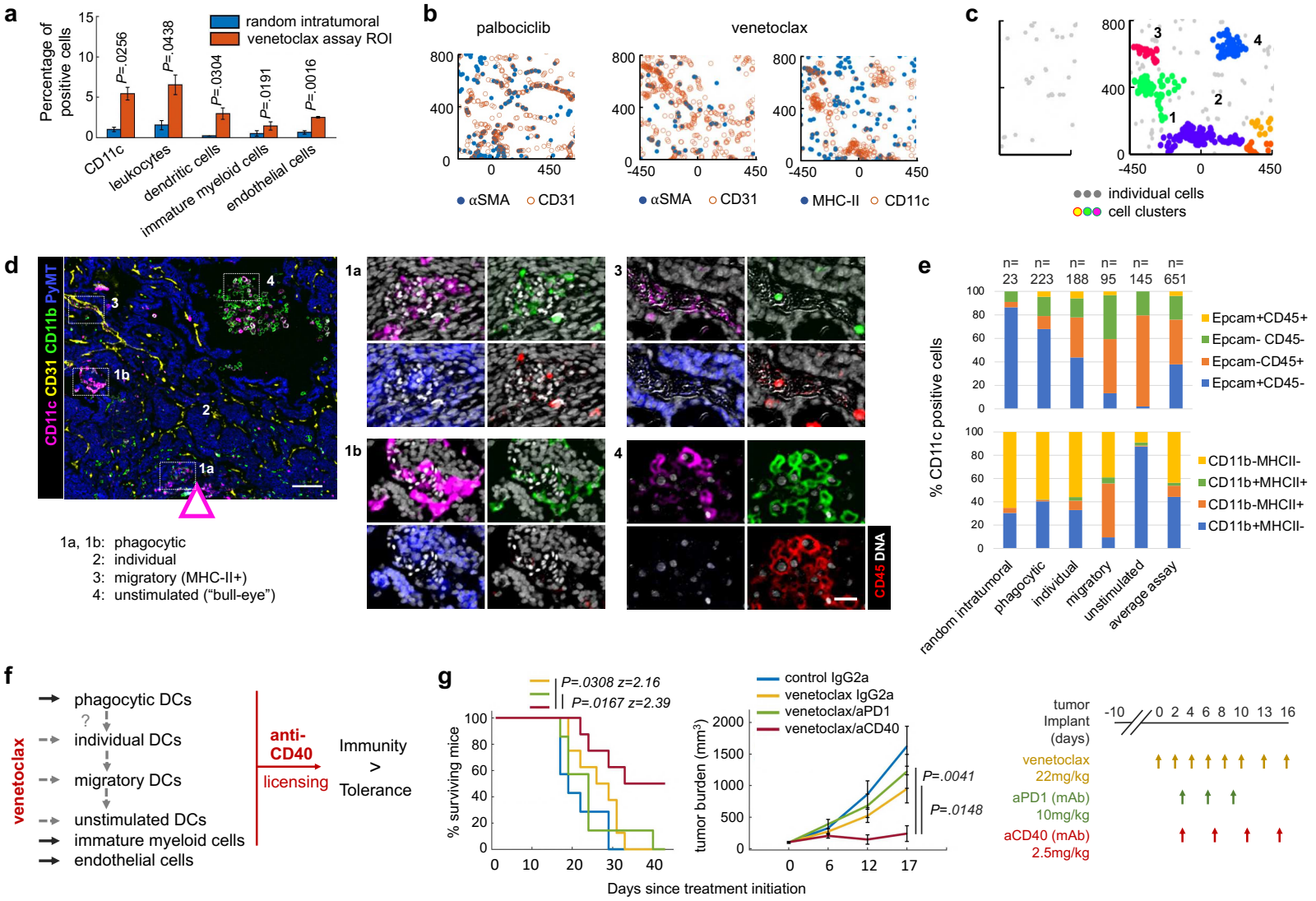

Fig. 3| Local TME changes induced by Venetoclax and whole animal studies testing the combination treatment efficacy with the predicted anti-CD40 immunotherapy. a, Quantification of single cell events using individual markers and standard cell types. Bars are mean ± s.e.; n=3 reservoirs. Significance was calculated by paired sample one tailed t-test. For quantification of all cells, see Extended Data Fig. 4e. **b,** Marker co-expression in XY coordinates in the palbociclib (left) and venetoclax (mid, right) assay area. Each color-coded dot represents a marker positive cell. Coordinate [0,0] identifies the drug source. The direction of the drug release is upward. **c,** Distance-based cluster analysis of CD11c positive cells as a set of XY coordinates in random intratumoral (left) and venetoclax assay (right) regions. Clusters are displayed in randomized colors if at least 10 cells are present within maximum distance range 50μm; individual cells not meeting this criterium are shown as light gray points. **d,** Sample composite image of the key response markers at the venetoclax well. Arrow indicates the source and direction of the drug release. Numbered hashed boxes define the magnified area on the right where individual markers are overlayed on the DNA signal (in white). Scale bar 100μm (left); and 30μm (right). **e,** Percentages of Epcam and CD45 (top) and CD11b and MHC-II (bottom) positive cells within morphologically different CD11c + DCs presented as a stack bar graph. The number of cells analyzed (n) is shown. Two to three ROIs from two venetoclax samples were summed per each zone. **f,** Venetoclax model of response presented as an influence diagram with sites of intervention using immunotherapy depicted in red. The relation of morphologically distinct and spatially separate CD11c DC clusters remains unclear (gray dashed arrows). **g,** Survival rates (left) and tumor burden measurements (right) of mice bearing E0771 tumors after systemic treatment using drugs as color-coded in the line graphs. Shown is mean ± s.e.; n=7-8 mice per group. Significance was calculated by log-rank (Mantel-Cox) and by an unpaired two-tailed t-test with equal variance for survival and tumor burden rate, respectively. For results using anti-PD-1 and anti-CD40 monotherapy see Fig. 6c.

Fig. 4

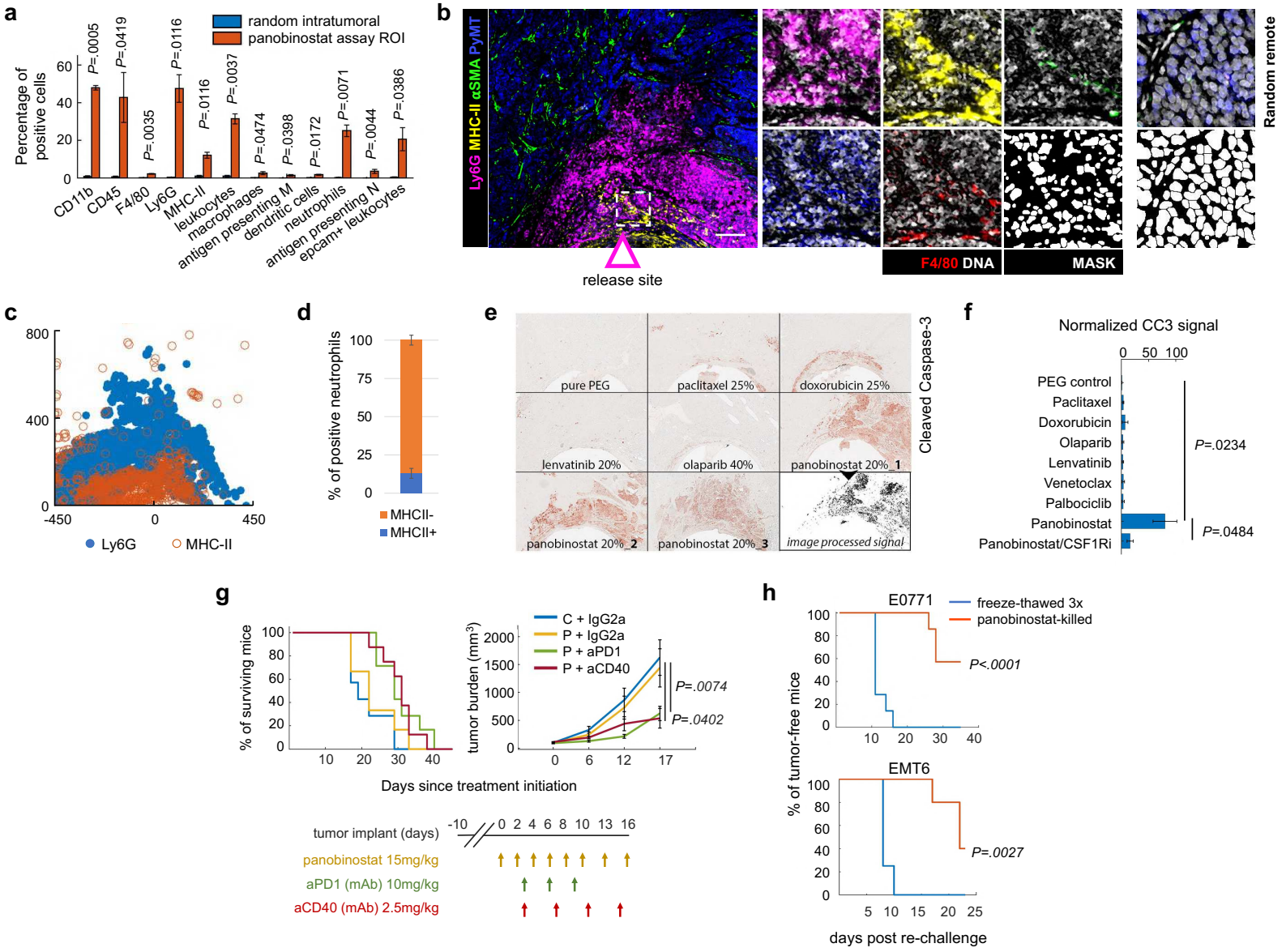

Fig. 4| Local effects of panobinostat and whole animal studies testing induction of anti-tumor immunity in mouse mammary carcinoma. a, Quantification of single cell events using individual markers and standard cell types. Bars are mean ± s.e.; n=3 reservoirs. Significance was calculated by paired sample one tailed t-test. For quantification of all cell, see Extended Data Fig. 5a. **b,** Sample composite image of the key response markers at the panobinostat well. A dashed box defines the magnified area (right), which shows F4/80 staining in red and DNA signal and DNA-derived mask in white. Scale bar, 100μm. **c,** Marker co-expression in XY coordinates. Each dot represents a marker positive cell. Coordinate [0,0] identifies the drug source. The direction of the drug release is upwards. **d,** Percentage of MHC-II+ neutrophils. Shown is mean ± s.e.; n=3 panobinostat reservoirs. **e,** CC3 IHC image of a sectioned tissue surrounding the IMD at depicted targeted agents and chemotherapies. Three replicates are presented for the most potent death-inducing drug, panobinostat. A computationally processed CC3 signal is shown as a binary image. **f,** Quantification of PEG normalized average mean CC3 intensity (px value) in the assay region. The graph shows mean ± s.e; n=3 wells per treatment; significance was calculated using an independent two-sample t-test with equal variance. **g,** Survival rates (left) and tumor burden measurements (right) of mice bearing E0771 tumors after systemic treatment using control diluent (C), panobinostat (P), anti-PD1, anti-CD40 and IgG2a isotype control monoclonal antibody. Shown is mean ± s.e.; n=7-8 mice per group. Significance was calculated by log-rank (Mantel-Cox) and by an unpaired two-tailed t-test with equal variance for survival and tumor burden rate, respectively. For results using anti-PD-1 and anti-CD40 monotherapy see Fig. 6c. Treatment dose and schedule is presented. **h,** Induction of anti-tumor immunity measured in a vaccination study using panobinostat treated cells and negative control (cells killed by three freeze/thaw cycles). Line graphs show percentages of mice free from palpable tumors. The P-value was calculated by log-rank (Mantel-Cox) test. n=7 per each group for E0771 model; and n=4 (control) and n=5 (experimental) for EMT6 model, respectively.

Fig. 5

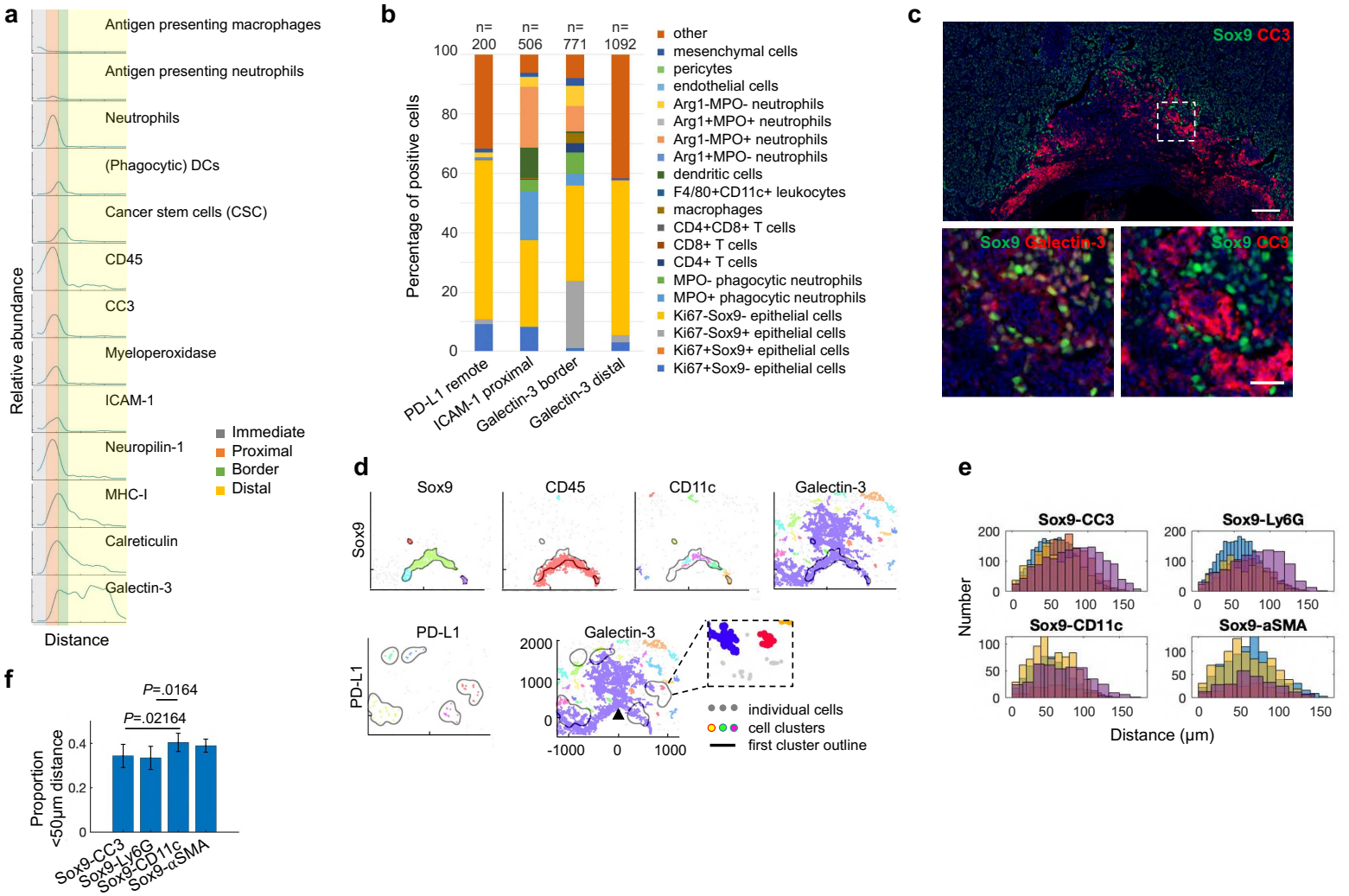

Fig. 5| Spatial single cell analyses of immunogenic cell death biomarkers and associated resistance mechanisms. a, Profile plot of the relative abundance of standard cell types and individual biomarkers with distance from the well. Assay zones are color-coded in the legend; profile area is shown in Extended Data Fig. 6a. **b,** Percentages of cells expressing biomarkers of ICD on standard cell types presented in form of a stack bar graph. The number of cells quantified (n) is presented. **c,** A composite image showing mutually exclusive staining of Sox9 and CC3; and co-expression of Sox9 with galectin-3 (bottom left image). Scale bar 100μm and 25μm for top and bottom images, respectively. **d,** Distance-based clustering of depicted marker positive cells in XY coordinates with overlay (black line) with Sox9 (top) and PD-L1 cluster border (bottom), respectively. Individual clusters were identified by a minimum 10 cells within a maximum 50μm distance for all but PD-L1 marker which clustered with a maximum distance set to 150μm. **e,f,** Number of Sox9+ pairwise distances with other marker positive cells presented in form of a histogram, e; and bar graph showing average proportion of Sox9 pairwise distances which were less than 50μm, h. n=4 ROIs of 175μm diameter in the border assay zone. Significance was determined by paired two tailed t test.

Fig. 6

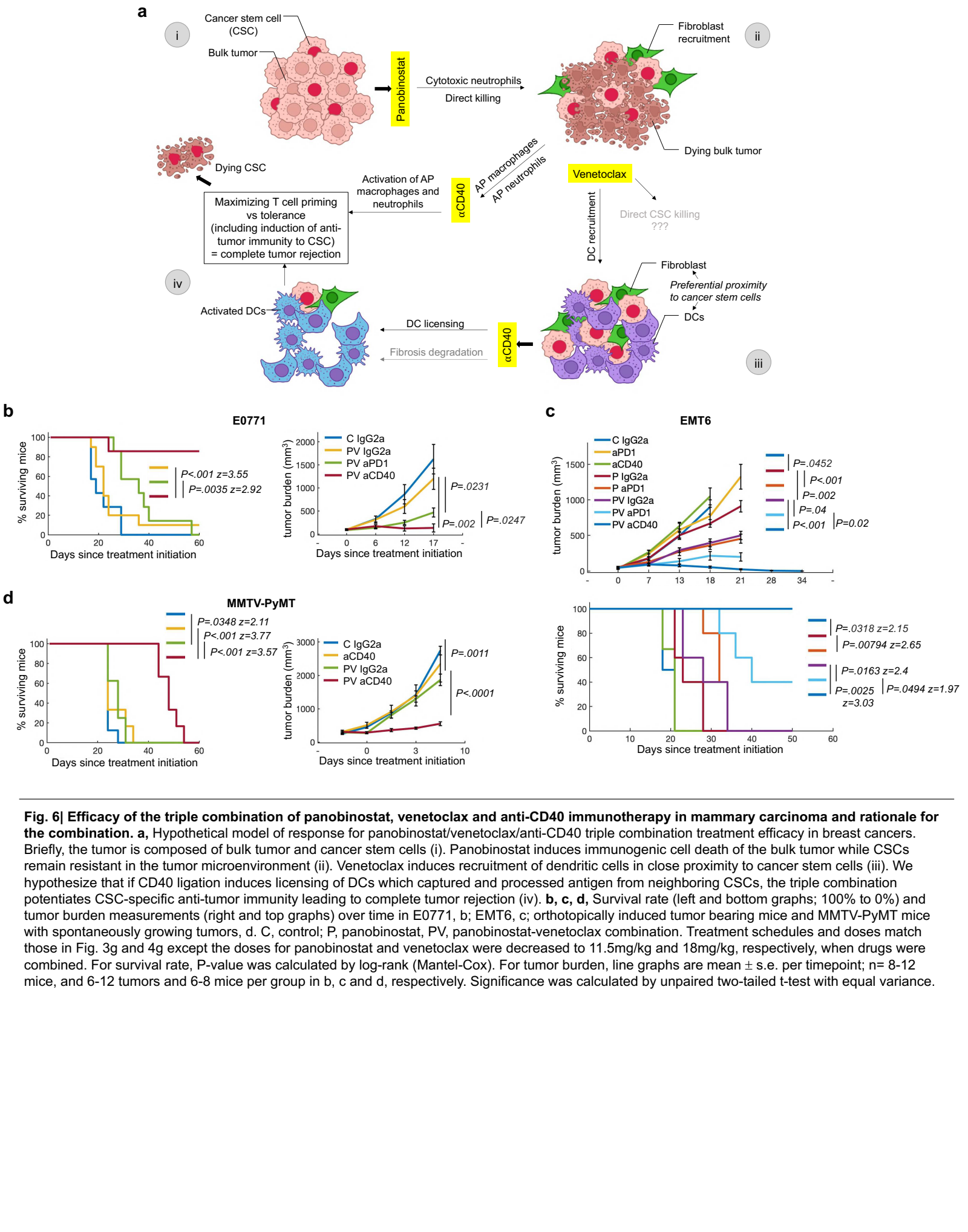

Fig. 6| Efficacy of the triple combination of panobinostat, venetoclax and anti-CD40 immunotherapy in mammary carcinoma and rationale for the combination. a, Hypothetical model of response for panobinostat/venetoclax/anti-CD40 triple combination treatment efficacy in breast cancers. Briefly, the tumor is composed of bulk tumor and cancer stem cells (i). Panobinostat induces immunogenic cell death of the bulk tumor while CSCs remain resistant in the tumor microenvironment (ii). Venetoclax induces recruitment of dendritic cells in close proximity to cancer stem cells (iii). We hypothesize that if CD40 ligation induces licensing of DCs which captured and processed antigen from neighboring CSCs, the triple combination potentiates CSC-specific anti-tumor immunity leading to complete tumor rejection (iv). **b, c, d,** Survival rate (left and bottom graphs; 100% to 0%) and tumor burden measurements (right and top graphs) over time in E0771, b; EMT6, c; orthotopically induced tumor bearing mice and MMTV-PyMT mice with spontaneously growing tumors, d. C, control; P, panobinostat, PV, panobinostat-venetoclax combination. Treatment schedules and doses match those in Fig. 3g and 4g except the doses for panobinostat and venetoclax were decreased to 11.5mg/kg and 18mg/kg, respectively, when drugs were combined. For survival rate, P-value was calculated by log-rank (Mantel-Cox). For tumor burden, line graphs are mean ± s.e. per timepoint; n= 8-12 mice, and 6-12 tumors and 6-8 mice per group in b, c and d, respectively. Significance was calculated by unpaired two-tailed t-test with equal variance.

Supplementary Files

This is a list of supplementary files associated with this preprint. Click to download.

- MIMANBTSupplementaryinformationfiles.pdf